

Massive Scalar Field Perturbations of Black Holes Surrounded by Dark Matter

Ramón Bécar,^{1,*} P. A. González,^{2,†} Eleftherios Papantonopoulos,^{3,‡} and Yerko Vásquez^{4,§}

¹*Departamento de Ciencias Matemáticas y Físicas, Universidad Católica de Temuco*

²*Facultad de Ingeniería y Ciencias, Universidad Diego Portales,
Avenida Ejército Libertador 441, Casilla 298-V, Santiago, Chile.*

³*Department of Physics, National Technical University of Athens, Zografou Campus GR 157 73, Athens, Greece.*

⁴*Departamento de Física, Facultad de Ciencias, Universidad de La Serena,
Avenida Cisternas 1200, La Serena, Chile.*

(Dated: March 5, 2024)

We consider scalar field perturbations in the background of black holes immersed in perfect fluid dark matter (PFDM). We find, by using the sixth order Wentzel-Kramers-Brillouin (WKB) approximation, that the longest-lived modes are the ones with higher angular number, for a scalar field mass smaller than a critical value, known as anomalous decay rate of the quasinormal modes, while that beyond this critical value the behaviour is inverted. Moreover, we show that it is possible to recover the real part of the quasinormal frequencies (QNFs), the imaginary part of the QNFs, and the critical scalar field mass, of the Schwarzschild background for different values of the PFDM intensity parameter k , respectively. For values of k smaller than these values, the mentioned quantities are greater than the Schwarzschild background. However, beyond of these values of k , these quantities are smaller than the Schwarzschild background.

Contents

I. Introduction	2
II. The setup of the theory	3
III. Scalar field perturbations	4
IV. Photon sphere modes	7
V. Conclusions	12
A. Higher order derivatives of the potential	13
B. Dimensionless analysis.	18
Acknowledgments	20
References	20

*Electronic address: rbecar@uct.cl

†Electronic address: pablo.gonzalez@udp.cl

‡Electronic address: lpapa@central.ntua.gr

§Electronic address: yvasquez@userena.cl

I. INTRODUCTION

The recent observations of gravitational waves (GWs) produced as a result of relativistic collision of two compact objects, opened up the possibility of studying the nature and the properties of compact objects. In the near future, following the recent LIGO detections [1]-[5], GW astronomy will provide us a better understanding of the gravitational interaction and astrophysics of these objects. The recent observations do not yet probe the detailed structure of spacetime of compact objects beyond the photon sphere; however, one expects that the properties of these objects will be revealed in the years to come with future GW observations. In particular, the expectation is to precisely detect the ringdown phase, which is governed by a series of damped oscillatory modes at early times, named quasinormal modes (QNMs) [6]-[9]. It is expected that the future GW observations will give some information on the nature and physics of the near-horizon region of black holes (BHs). The existence of any structure at near-horizon scales would generate a series of “echoes” of the primary gravitational wave signal, produced during the ringdown phase [10, 11].

In General Relativity one of the most important compact object is the BH. One of the most distinguishable feature of BHs is the event horizon. The event horizon which is a causal boundary, does not allow us to go inside the BH. Black holes in our Universe may be affected by astronomical environments, such as the dark matter (DM) near the BHs [12]-[14]. It is believed that 90% of galaxies are composed of DM [15]. The abnormally high velocities of stars at the outskirts of galaxies imply that visible disks of galaxies are immersed in a much larger roughly spherical halo of DM [16, 17]. The DM does not interact with the electromagnetic field and therefore the propagation of light is possible inside the dark matter halo. Some studies to learn whether the black hole shadow could be affected by the tidal forces induced by the invisible matter have been performed in [18–20]. However, the results look highly model-dependent, due to a particular equation of state for the dark matter was considered. Then the most reliable way to detect dark matter outside the BH is to study the gravitational wave signal, produced during the ringdown phase generating a series of echoes. Various models of black holes surrounded by dark matter have been studied [21]-[24].

On the other hand, recent astrophysical observations show an accelerating expansion of Universe [25], implying the presence of a state with negative pressure. The negative pressure could be originated from the presence of barotropic perfect fluid which corresponds to the dark energy or to the presence of a cosmological constant. The state equation is given by the relation between the pressure p and the energy density ρ , $w = p/\rho$ and the recent observations suggest that the equation of state lies in a narrow strip around $w = -1$ [26, 27], where $w = -1$ corresponds to a cosmological constant Λ and $w < -1$ is allowed [28, 29]. Considering that the Universe is filled with a barotropic perfect fluid corresponding to dark energy, an equation of state $w < -1$ can be realized with the presence of a phantom field. The phantom dark energy has the property that the dominant energy condition is violated so that the energy density and curvature may grow to infinity in a finite time, which is referred to a Big Rip singularity [29, 30]. The introduction of dark matter may explain the discrepancy between the predicted rotation curves of galaxies when only including luminous matter and the actual (observed) rotation curves which differ significantly [31–33].

A spherical halo of dark matter around the Schwarzschild BH has been considered for testing the gravitational response of black holes in the astrophysical environment [34–36], and also to study the shadow [37]. The dark matter possesses some mass which can be modelled as an additional effective mass in the mass function of a BH. Then one expects that the ringdown profile to be modified due to new physics near the surface/event horizon and echoes to be generated due to matter at some distance from the black hole. This allows us to understand how the echoes of the surface of the BH are affected by the astrophysical environment at a distance. We expect that the straightforward calculations for the time-domain profiles of such a system to support the expectations that if the echoes are observed, they should most probably be ascribed to some new physics near the event horizon rather than some “environmental” effect. An exact and fully relativistic solution of the Einstein field equations was discussed in [38] which describes a black hole in the center of an anisotropic dark matter halo without the need of adding any Newtonian potential for the dark matter, and metric perturbations in these spacetimes were also studied [39].

Static spherically-symmetric exact solutions of Einstein equations with the quintessential matter having negative equation of state surrounding a black hole charged or not was presented in [40, 41]. A condition of additivity and linearity in the energy-momentum tensor was introduced, allowing to get the known solutions for the electromagnetic static field, implying a relativistic relation between the energy density and pressure. A real phantom field minimally coupled to gravity was introduced in [42], with the aim to investigate the possibility that the galactic dark matter exists in an scenario with a phantom field responsible for the dark energy, where there is a static and spherical approximate solution for this kind of the galaxy system with a supermassive black hole at its center. The phantom field defined in an effective theory is valid only at low energies, in order to avoid the well-known quantum instability of the vacuum at high frequencies.

The aim of this work is to study the propagation of massive scalar fields in a BH spacetime surrounded by perfect fluid dark matter (PFDM) for highest values of ℓ in order to see if there is an anomalous decay rate of QNMs for the photon sphere modes [43]. The QNMs give an infinite discrete spectrum which consists of complex frequencies, $\omega = \omega_R + i\omega_I$, where the real part ω_R determines the oscillation timescale of the modes, while the complex part ω_I

determines their exponential decaying timescale. If the background consists of Schwarzschild and Kerr BHs it was found that for gravitational perturbations the longest-lived modes are always the ones with lower angular number ℓ . This is understood from the fact that the more energetic modes with high angular number ℓ would have faster decaying rates. The anomalous behaviour occurs when the longest-lived modes are the ones with higher angular number and this can occur with a massive probe scalar field. There is a critical mass of the scalar field where the behaviour of the decay rate of the QNMs is inverted and can be obtained from the condition $Im(\omega)_\ell = Im(\omega)_{\ell+1}$ in the *eikonal* limit, that is when $\ell \rightarrow \infty$. The anomalous behaviour in the quasinormal frequencies (QNFs) is possible in asymptotically flat, in asymptotically dS and in asymptotically AdS spacetimes; however, we observed that the critical mass exist for asymptotically flat and for asymptotically dS spacetimes and it is not present in asymptotically AdS spacetimes for large and intermediate BHs. Moreover, such behaviour have been studied for scalar fields [44–53] as well as charged scalar fields [54, 55] and fermionic fields [56]. The anomalous decay in accelerating black holes was studied in [57].

The QNMs for a massless scalar field and their connection to the shadow radius in the background of a modified Schwarzschild BH was studied in [58]. The modification of the background BH was due to the presence of the PFDM surrounding the BH encoded by the parameter k . It was shown that the QNM spectra deviates from those of Schwarzschild BH due to the presence of the PFDM. Moreover, for any $k > 0$, the real part and the absolute value of the imaginary part of QNFs increases and this means that the field perturbations in the presence of PFDM decays more rapidly compared to Schwarzschild vacuum BH. Also, it was shown that there exists a reflecting point k_0 corresponding to maximal values for the real part of QNM frequencies. Namely, as the PFDM parameter k increases in the interval $k < k_0$, the QNFs increases and reach their maximum values at $k = k_0$. Also, it was shown that k_0 is also a reflecting point for the shadow radius. In the physical context, QNFs are associated with the value of the effective potential and its derivatives evaluated at its maximum point. For asymptotically flat black holes, this radius corresponds to the radius of the photon sphere or the radius of unstable null geodesics. Furthermore, as shown in [43], utilizing the WKB approximation and establishing the connection between unstable null geodesics and QNFs in the eikonal limit, the following relation was found for the real part of the QNFs $\omega_{real} = l\sqrt{\frac{f(r_c)}{r_c^2}}$, where r_c is the radius of unstable null geodesics or the photon sphere. Additionally, it was demonstrated in [58–61] that the black hole shadow radius can be related to the real part of QNFs in the eikonal limit: $\omega_{real} = \frac{l}{R_s}$, where $R_s = \frac{r_c}{\sqrt{f(r_c)}}$. As indicated in the article [58], the shadow radius attains its lowest value for $k = k_0 = 0.81$, which, according to the expression for ω_{real} , corresponds to the largest quasinormal oscillation (real part). This aligns with the results obtained through the WKB method. It is worth noting that if the event horizon decreases, it will lead to a reduction in the shadow radius and, consequently, higher values for the oscillation frequencies.

However, the analysis in [58] was carried out for low values of ℓ , and it is known that the WKB method provides better accuracy for larger ℓ (and $\ell > n$ where n is the overtone). In this study, we consider larger values of ℓ , and we show that there is a value of the parameter k , for which the real part of the QNFs is maximum, which is associated with a reflecting point in the context of BH shadow. Additionally, our results show that there is a value of the parameter k , for which the absolute value of the imaginary part of the QNFs is maximum. As we will see, there is a value of $k \neq 0$, that reproduces the real and the imaginary part of the QNFs of the Schwarzschild background separately, but there is not a value of k that can reproduce the same QNF that the Schwarzschild background. Also, we show the existence of an anomalous behaviour of the decay rate for the background considered. Moreover, there is a value of $k \neq 0$, that reproduces the critical scalar field mass of the Schwarzschild background.

The work is organized as follows. In Sec. II, we give the setup of the theory. Then, in Sec. III we study the scalar perturbations, and in Sec. IV we study the photon sphere modes. Finally, conclusions and final remarks are presented in Sec. V.

II. THE SETUP OF THE THEORY

One of the first works that discussed static spherically-symmetric exact solutions of Einstein equations with the dark matter surrounding a black hole was discussed in [40]. A condition of additivity and linearity in the energy-momentum tensor was introduced, which allows one to get correct limits to the known solutions implying the relativistic relation between the energy density and pressure. The solution which was found is

$$ds^2 = \left[1 - \frac{r_g}{r} - \sum_n \left(\frac{r_n}{r} \right)^{3w_n+1} \right] dt^2 - \frac{dr^2}{\left[1 - \frac{r_g}{r} - \sum_n \left(\frac{r_n}{r} \right)^{3w_n+1} \right]} - r^2(d\theta^2 - \sin^2\theta d\phi^2), \quad (1)$$

where $r_g = 2M$, M is the black hole mass, r_n are the dimensional normalization constants, and w_n are the dark matter state parameters

$$p_n = w_n \rho_n . \quad (2)$$

This work was further extended in [41] in which a scalar field was introduced. Then the state describing the dark matter with the negative pressure was considered as a perfect fluid approximation of a scalar field with an appropriate potential. So, introducing a scalar field φ with the Lagrangian equal to

$$\mathcal{L} = \frac{1}{2} g^{\mu\nu} \partial_\mu \varphi \partial_\nu \varphi - V(\varphi) , \quad (3)$$

with identification

$$\rho_{DM} = -g^{tt} [\partial_r \varphi(r)]^2 ,$$

the dark matter modified metric (1) was reproduced.

The possibility that a phantom field is responsible for the dark matter was further investigated in [42]. A spherically approximate solution of a dark matter galaxy was obtained with a supermassive black hole at its center. The solution of the metric functions is satisfied with $g_{tt} = -g_{rr}^{-1}$ and the observation of the rotational stars moving in circular orbits in a spiral galaxy constrained the background of the phantom field to be spatially inhomogeneous having an exponential potential.

The action of real phantom field minimally coupled to gravity was given by

$$S = \int d^4x \sqrt{-g} \left[\frac{R}{2\kappa^2} + \frac{1}{2} g^{uv} \partial_u \Phi \partial_v \Phi - V(\Phi) + \mathcal{L}_m \right] , \quad (4)$$

where R is the Ricci scalar, $\kappa^2 = 8\pi G$ being G the Newton constant, and $V(\phi)$ is the phantom field potential. The term \mathcal{L}_m account for the massive dark matter in the galaxy.

The black hole solution is described by the metric

$$ds^2 = -f(r) dt^2 + \frac{dr^2}{f(r)} + r^2 (d\theta^2 + \sin^2 \theta d\phi^2) , \quad (5)$$

where

$$f(r) = 1 - \frac{2M}{r} + \frac{k}{r} \ln\left(\frac{r}{|k|}\right) , \quad (6)$$

M is the black hole mass and k is a parameter describing the intensity of the PFDM. The above metric function is similar to the metric function with the parameter k specifying the presence of the phantom scalar field acting as its scalar charge. It was found that because the infalling phantom particles have a total negative energy, the accretion of the phantom energy is related to the decrease of the black hole mass.

Using (5) as the background metric with the metric function (6), massless scalar field and electromagnetic field perturbations were carried out in [58]. It was found that the presence of the PFDM parameter k results in a deviation of quasinormal mode spectra from those of Schwarzschild black hole and it was shown that the field perturbations in the presence of PFDM decay more rapidly compared to Schwarzschild vacuum black hole.

III. SCALAR FIELD PERTURBATIONS

We first show in Fig. 1, the behaviour of the event horizon radius r_h of the BH as a function of the parameter k (in the following we consider $k > 0$) using the metric function (6). We can observe that when the BH mass M increases, the event horizon radius increases. Also, the event horizon is minimum for $k = k_h = \frac{2M}{1+e}$. Namely, as the PFDM parameter k increases in the interval $k < k_h$, r_h decreases and reaches its minimum value at $k = k_h$. Then, for $k > k_h$, r_h increases when the parameter k increases. It is worth noting that there is a value of k , for which the event horizon radius is the same as the Schwarzschild BH, and beyond this value of k the event horizon is greater than the Schwarzschild background. The QNMs of scalar perturbations in the background of the metric (5) are given by the scalar field solution of the Klein-Gordon equation

$$\frac{1}{\sqrt{-g}} \partial_\mu (\sqrt{-g} g^{\mu\nu} \partial_\nu \varphi) = m^2 \varphi , \quad (7)$$

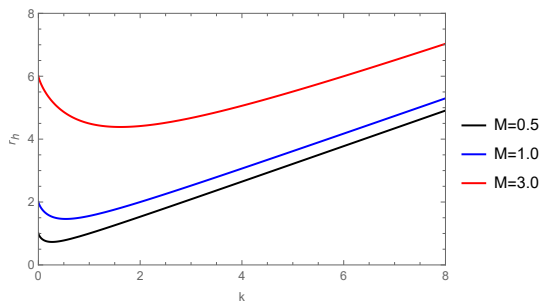


FIG. 1: The behaviour of the event horizon radius r_h as a function of the PFDM intensity parameter k . Black line for $M = 0.5$, blue line for $M = 1.0$, and red line for $M = 3.0$.

with suitable boundary conditions for a BH geometry. In the above expression m is the mass of the scalar field φ . Now, by means of the following ansatz

$$\varphi = e^{-i\omega t} R(r) Y(\Omega), \quad (8)$$

the Klein-Gordon equation reduces to

$$\frac{1}{r^2} \frac{d}{dr} \left(r^2 f(r) \frac{dR}{dr} \right) + \left(\frac{\omega^2}{f(r)} - \frac{\kappa^2}{r^2} - m^2 \right) R(r) = 0, \quad (9)$$

where we defined $-\kappa^2 = -\ell(\ell + 1)$, with $\ell = 0, 1, 2, \dots$, which represents the eigenvalues of the Laplacian on the two-sphere and ℓ is the multipole number. Now, defining $R(r) = \frac{F(r)}{r}$ and by using the tortoise coordinate r^* given by $dr^* = \frac{dr}{f(r)}$, the Klein-Gordon equation can be written as a one-dimensional Schrödinger-like equation

$$\frac{d^2 F(r^*)}{dr^{*2}} - V_{eff}(r) F(r^*) = -\omega^2 F(r^*), \quad (10)$$

with an effective potential $V_{eff}(r)$, which parametrically thought, $V_{eff}(r^*)$, is given by

$$V_{eff}(r) = \frac{f(r)}{r^2} (\kappa^2 + m^2 r^2 + f'(r)r). \quad (11)$$

In Fig. 2, we show its behaviour for different values of the parameters. Note that a barrier of potential occurs in each case, with its maximum value increasing when ℓ or m increases. However, for $0 < k \leq 0.81$ the maximum in the potential increases when k increases. But for $k > 0.81$, the maximum of the potential decreases when k increases, being possible to recover the height of the potential for the Schwarzschild case ($k \approx 3.50$), but with a larger event horizon.

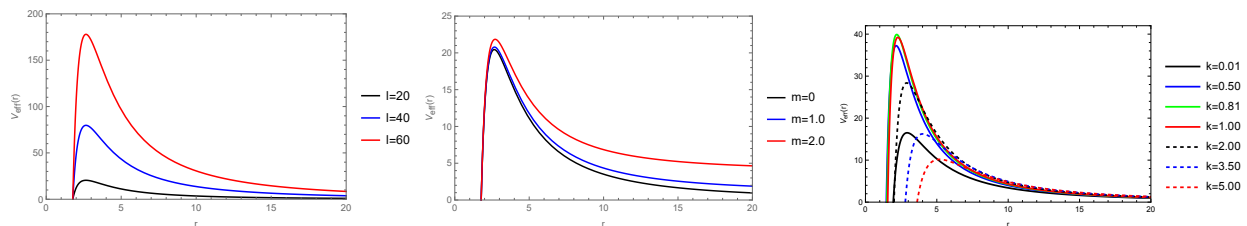


FIG. 2: The effective potential V_{eff} as a function of r , with $M = 1$. Left panel for massless scalar field $m = 0$, $k = 0.01$, and $\ell = 20, 40, 60$. Central panel for $\ell = 20$, $k = 0.01$, and $m = 0, 1.0, 2.0$. Right panel for $\ell = 20$, $m = 0$, and $k = 0.01, 0.50, 1.00, 2.00, 3.50, 5.00$.

The effective potential can be splitted as $V_{eff}(r) = V_{Sch}(r) + V_{dM}(r)$, where

$$V_{Sch}(r) = -\frac{(2M - r)(l(l + 1)r + m^2r^3 + 2M)}{r^4}, \quad (12)$$

$$V_{dM}(r) = \frac{k \left(\log\left(\frac{r}{k}\right) \left(-k \log\left(\frac{r}{k}\right) + k + (l^2 + l - 1)r + m^2r^3 + 4M\right) - 2M + r \right)}{r^4}. \quad (13)$$

In Fig. 3 we plot their behaviour. For $k=0.5$ (left panel), the event horizon is located at $r_h = 1.463$. Note that near the horizon the blue line representing to V_{Sch} is negative until $r = 2M$, and the red line representing to V_{dM} is positive. Beyond $r = 2M$, both potentials are positive (V_{Sch} , and V_{dM}). Then, for $k = 2.0$ (central panel), and $r > r_h$ with $r_h = 2.0$, both potentials are positive (V_{Sch} , and V_{dM}). Then, for $k = 5.0$ (right panel), and $r > r_h$ with $r_h = 3.618$, beyond the horizon the blue line (V_{Sch}) is positive, and the red line (V_{dM}) is negative. Beyond $V_{dM} = 0$, both potentials are positive (V_{Sch} , V_{dM}). It is worth mentioning that for large values of r , V_{dM} goes to zero, and $V_{eff}(r)$ goes to V_{Sch} .

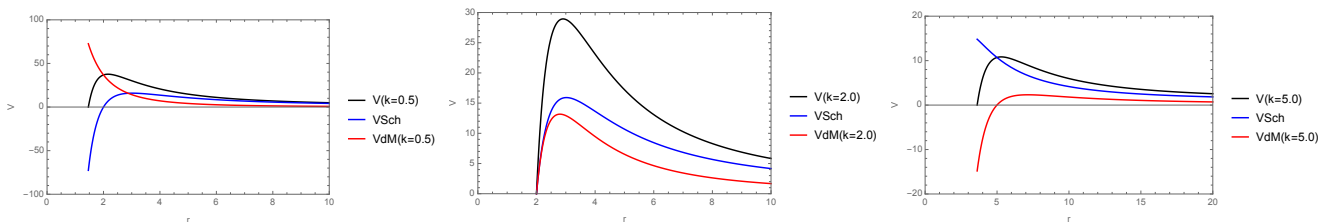


FIG. 3: The behaviour of the potentials V_{Sch} , V_{dM} and $V = V_{Sch} + V_{dM}$ as a function of r with $m = 1$, $M = 1$, and $\ell = 20$. Black line for V , blue line for V_{Sch} , and red line for V_{dM} . Left panel for $k = 0.5$, and $r_h = 1.463$, central panel for $k = 2.0$, and $r_h = 2$, and right panel for $k = 5.0$, and $r_h = 3.618$.

As we can see from the above figure at fixed value of the scalar field mass $m = 1$, at large distances the PFDM does not contribute and we recover the Schwarzschild black hole while near the horizon the k parameter of the PFDM plays a decisive role. Varying the parameter k , from $k = 0.5$ to $k = 5$ there is an interplay of the potentials from negative to positive values indicating how the PFDM from small to large values interacts with the Schwarzschild black hole.

In Fig. 4 we show the effect of the scalar field mass on the potential for the three cases previously analyzed ($k = 0.5, 2.0, 5.0$). We observe that the absolute value of each potential, $V_{eff}(r)$, V_{Sch} and V_{dM} increases, when the scalar field mass increases and this is happening near the horizon of the black hole. We also observe that the largest increase of the absolute value of each potential occurs at intermediate values of the PFDM parameters k . Also, when $r \rightarrow \infty$ we find from Eqs. (11), (12), and (13), that the asymptotic behaviour of the potentials are given by $V_{eff}(r) \rightarrow m^2$, $V_{Sch} \rightarrow m^2$ and $V_{dM} \rightarrow 0$ as expected.

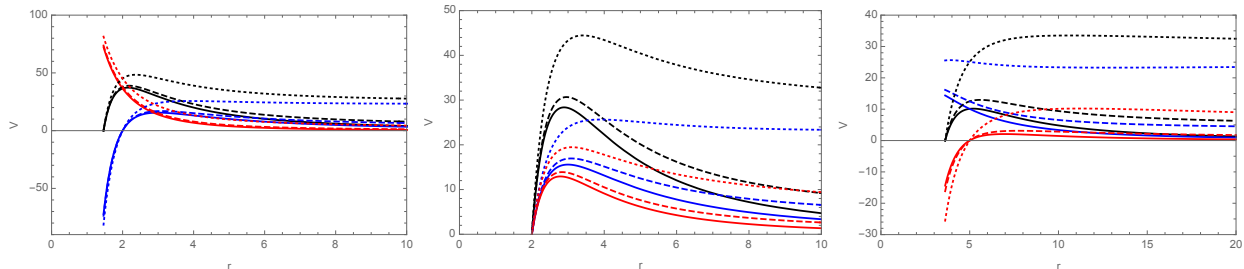


FIG. 4: The behaviour of the potentials V_{Sch} , V_{dM} and $V = V_{Sch} + V_{dM}$ as a function of r with $M = 1$, and $\ell = 20$. Black line for V , blue line for V_{Sch} , and red line for V_{dM} . Left panel for $k = 0.5$, and $r_h = 1.463$, central panel for $k = 2.0$, and $r_h = 2$, and right panel for $k = 5.0$, and $r_h = 3.618$. Continuous line for massless scalar field $m = 0$, dashed line for $m = 2.0$, and dotted line for $m = 5.0$.

IV. PHOTON SPHERE MODES

In this section, in order to get some analytical insight of the behaviour of the QNFs in the eikonal limit $\ell \rightarrow \infty$, we use the method based on the Wentzel-Kramers-Brillouin (WKB) approximation initiated by Mashhoon [62] and by Schutz and Iyer [63]. Iyer and Will computed the third order correction [64], and then it was extended to the sixth order [65], and recently up to the 13th order [66], see also [67].

This method has been used to determine the QNFs for asymptotically flat and asymptotically de Sitter black holes. This is due to the WKB method can be used for effective potentials which have the form of potential barriers that approach to a constant value at the horizon and spatial infinity [9]. However, only the photon sphere modes can be obtained with this method. The QNMs are determined by the behaviour of the effective potential near its maximum value $V(r_{max}^*)$. The Taylor series expansion of the potential around its maximum is given by

$$V(r^*) = V(r_{max}^*) + \sum_{i=2}^{\infty} \frac{V^{(i)}}{i!} (r^* - r_{max}^*)^i, \quad (14)$$

where

$$V^{(i)} = \frac{d^i}{dr^{*i}} V(r^*)|_{r^*=r_{max}^*}, \quad (15)$$

corresponds to the i -th derivative of the potential with respect to r^* evaluated at the position of the maximum of the potential r_{max}^* . Using the WKB approximation up to third order beyond the eikonal limit, the QNFs are given by the following expression [68]

$$\omega^2 = V(r_{max}^*) - 2iU, \quad (16)$$

where

$$U = N\sqrt{-V^{(2)}/2} + \frac{i}{64} \left(-\frac{1}{9} \frac{V^{(3)2}}{V^{(2)2}} (7 + 60N^2) + \frac{V^{(4)}}{V^{(2)}} (1 + 4N^2) \right) + \frac{N}{2^{3/2}288} \left(\frac{5}{24} \frac{V^{(3)4}}{(-V^{(2)})^{9/2}} (77 + 188N^2) \right. \\ \left. + \frac{3}{4} \frac{V^{(3)2}V^{(4)}}{(-V^{(2)})^{7/2}} (51 + 100N^2) + \frac{1}{8} \frac{V^{(4)2}}{(-V^{(2)})^{5/2}} (67 + 68N^2) + \frac{V^{(3)}V^{(5)}}{(-V^{(2)})^{5/2}} (19 + 28N^2) + \frac{V^{(6)}}{(-V^{(2)})^{3/2}} (5 + 4N^2) \right),$$

and $N = n + 1/2$, with $n = 0, 1, 2, \dots$, is the overtone number. The imaginary and real part of the QNFs can be written as

$$\omega_I^2 = -(Im(U) + V/2) + \sqrt{(Im(U) + V/2)^2 + Re(U)^2}, \quad (17)$$

$$\omega_R^2 = -Re(U)^2/\omega_I^2, \quad (18)$$

respectively, where $Re(U)$ is the real part of U and $Im(U)$ its imaginary part. Now, defining $L^2 = \ell(\ell + 1)$, we find that for large values of L , the maximum of the potential is approximately at

$$r_{max} \approx r_0 + \frac{1}{L^2} r_1, \quad (19)$$

where

$$r_0 = \frac{3}{2} k W \left(\frac{2}{3} e^{\frac{2M}{k} + \frac{1}{3}} \right), \quad (20)$$

$W(x)$ is the Lambert function, and

$$r_1 = \frac{2r_0(k^2 + 12kM + 16M^2 - 2(2k + 3M)r_0 + m^2(k + 2M)r_0^3) + 2kr_0 \log(\frac{r_0}{k})(-6k - 16M + 3r_0 - m^2r_0^3 + 4k \log(\frac{r_0}{k}))}{2r_0(2k - 6M + 4r_0 + 3k \log(\frac{r_0}{k}))}. \quad (21)$$

So, the potential evaluated at r_{max}^* , is given by

$$V(r_{max}^*) \approx \frac{(-2M + r_0 + k \log(\frac{r_0}{k}))}{r_0^3} L^2 + \frac{1}{9r_0^4} \left(-3(29k^2 + 66kM + 60M^2) + 4(-7k + 6M)r_0 - 14r_0^2 \right. \\ \left. -18m^2(k + 2M)r_0^3 + 3m^2r_0^4 + 3k \log(\frac{r_0}{k})(33k + 60M - 4r_0 + 6m^2r_0^3 - 15k \log(\frac{r_0}{k})) \right. \\ \left. + \frac{(3k + 2r_0)(61k^2 + 4r_0^2(7 + 3m^2r_0^2) + kr_0(82 + 15m^2r_0^2))}{2k + 6M - 4r_0 + 3k \log(\frac{r_0}{k})} \right). \quad (22)$$

The higher order derivatives $V^{(i)}(r_{max}^*)$ with $i = 2, 3, 4, 5, 6$ are presented in appendix A. So, by using these terms, and Eq. (A11), we can find an analytical expression for the critical scalar field mass m_c , which is too lengthy to be presented here, because it is obtained from the term proportional to $1/L^2$ in ω . However, we plot its behaviour as a function of k in Fig. 5. We can observe that when the BH mass M increases the critical scalar field mass decreases. Also, there is a value of k_c corresponding to a maximal value for the critical scalar field mass. Namely, as the PFDM parameter k increases in the interval $k < k_c$, m_c increases and reach their maximum values at $k = k_c$. Then, for $k > k_c$ the m_c decreases when the parameter k increases. Remarkably, there is a value of the PFDM parameter k , for which the critical scalar field mass is the same that for the Schwarzschild BH, beyond this value of k the critical scalar field mass is smaller than of the Schwarzschild background. This behaviour of the scalar field mass m and the PFDM parameter k indicates that these is an interplay between the real matter and the phantom matter effecting the mass of the background Schwarzschild black hole.

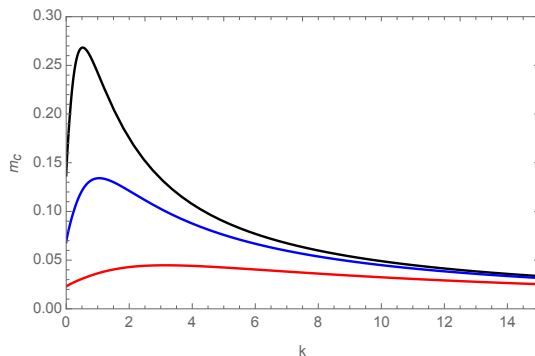


FIG. 5: The behaviour of the critical scalar field mass m_c for the fundamental mode $n = 0$ as a function of k . Black line for $M = 0.5$, blue line for $M = 1.0$, and red line for $M = 3.0$.

Now, we plot in Fig. 6 the behaviour of the real and imaginary part of the QNFs as a function of the PFDM intensity parameter k , separately. We can observe that there is a value of the parameter $k_0 \approx 0.81$, for which the real part of the QNFs is maximum, which is associated with a reflecting point in the context of BH shadow. Namely, as the PFDM parameter k increases in the interval $k < k_0$, the QNF increases and reach their maximum values at $k = k_0$, as was point out in Ref. [58] for low values of ℓ . Then, for $k > k_0$ the real part of the QNF decreases when the parameter k increases. Remarkably, there is a value of the PFDM parameter k , for which the real part of the QNF is the same that for the Schwarzschild BH, beyond this value of k the frequency of oscillation is smaller than the Schwarzschild case. Also, a similar behaviour occurs for the absolute value of the imaginary part of the QNF. Also, it is possible to observe that for massive scalar field, the real part of the QNFs increases and the absolute value of the imaginary part of the QNFs decreases in comparison with massless scalar field.

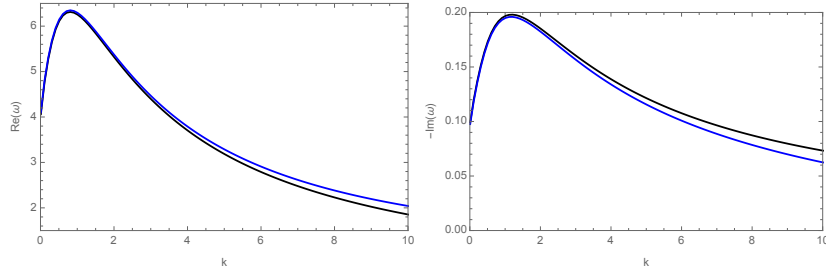


FIG. 6: The behaviour of $Re(\omega)$ (left panel), and $Im(\omega)$ (right panel) for the fundamental mode ($n = 0$) as a function of the PFDM intensity parameter k with $M = 1$, and $\ell = 20$. Black line for massless scalar field ($m = 0$), and blue line for massive scalar field ($m = 1.0$).

We show in the following tables that the real part of the QNFs have a maximum at $k_0 \approx 0.81$, and this value does not depend on n (see Table I) or ℓ (see Table II). Note also that the imaginary part of the QNFs have a maximum at $k \approx 1.19$, and this value also does not depend on n (see Table III) or ℓ (see Table IV).

TABLE I: QNFs for $M = 1$, $\ell = 20$, $m = 0$ and different values of k , and n .

k	$n = 0$	$n = 1$	$n = 2$
0.80	$6.312337229 - 0.1915424746i$	$6.305063321 - 0.5749004929i$	$6.290555033 - 0.9590774523i$
0.81	$6.312403646 - 0.1919177167i$	$6.305095686 - 0.5760279567i$	$6.290519578 - 0.9609623546i$
0.82	$6.312128105 - 0.192279291i$	$6.304786728 - 0.577114394i$	$6.290144067 - 0.9627788027i$

TABLE II: The fundamental QNFs for $M = 1$, $m = 0$ and different values of k , and ℓ .

k	$\ell = 20$	$\ell = 40$	$\ell = 60$
0.80	$6.312337229 - 0.1915424746i$	$12.46960361 - 0.191520156i$	$18.62711699 - 0.1915159121i$
0.81	$6.312403646 - 0.1919177167i$	$12.46973043 - 0.1918952382i$	$18.6273052 - 0.1918909639i$
0.82	$6.312128105 - 0.192279291i$	$12.46918178 - 0.1922566546i$	$18.62648438 - 0.1922523502i$

TABLE III: QNFs for $M = 1$, $\ell = 20$, $m = 0$ and different values of k , and n .

k	$n = 0$	$n = 1$	$n = 2$
1.18	$6.137647315 - 0.1980102076i$	$6.129473798 - 0.5943544216i$	$6.11317502 - 0.991669935i$
1.19	$6.129636142 - 0.1980113209i$	$6.121448324 - 0.5943587095i$	$6.105121121 - 0.9916802457i$
1.20	$6.121513845 - 0.1980059472i$	$6.113312125 - 0.5943435188i$	$6.096957289 - 0.9916580336i$

TABLE IV: The fundamental QNFs for $M = 1$, $m = 0$ and different values of k , and ℓ .

k	$\ell = 20$	$\ell = 40$	$\ell = 60$
1.18	$6.137647315 - 0.1980102076i$	$12.12437267 - 0.1979831253i$	$18.1113699 - 0.1979779755i$
1.19	$6.129636142 - 0.1980113209i$	$12.10854406 - 0.1979841471i$	$18.08772422 - 0.1979789798i$
1.20	$6.121513845 - 0.1980059472i$	$12.09249597 - 0.1979786833i$	$18.06375069 - 0.197973499i$

Now, we show the relation of QNFs to the location of the horizon in Fig. 7. We can observe a maximum value of the real part of the QNFs at $r_h \approx 1.502$, and for the imaginary part at $r_h \approx 1.622$. Also, it is possible to observe that for massive scalar fields, the real part of the QNFs increases and the absolute value of the imaginary part of the QNFs decreases in comparison to massless scalar fields.

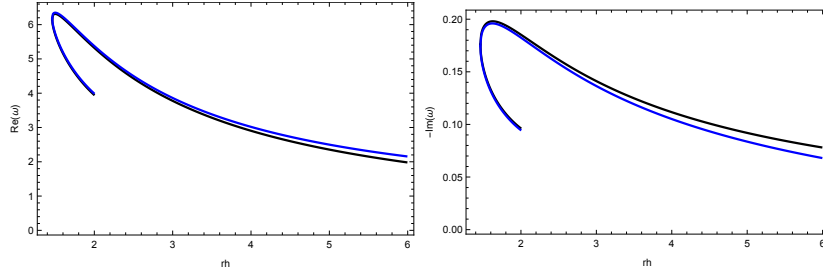


FIG. 7: The behaviour of $Re(\omega)$ (left panel), and $Im(\omega)$ (right panel) for the fundamental mode ($n = 0$) as a function of the event horizon r_h with $M = 1$, and $\ell = 20$. Black line for massless scalar field ($m = 0$), and blue line for massive scalar field ($m = 1.0$).

Now, in order to show the anomalous behaviour, we plot in Figs. 8, and 9, the behaviour of $-Im(\omega)$ as a function of m by using the 6th order WKB method for $n = 0$, and $n = 1$, respectively. We can observe an anomalous decay rate, i.e, for $m < m_c$, the longest-lived modes are the ones with highest angular number ℓ ; whereas, for $m > m_c$, the longest-lived modes are the ones with smallest angular number. Also, when the overtone number n increases the parameter m_c increases. Also, it is possible to observe that the behaviour of the critical scalar field mass with respect to the parameter k agrees with Fig. 5.

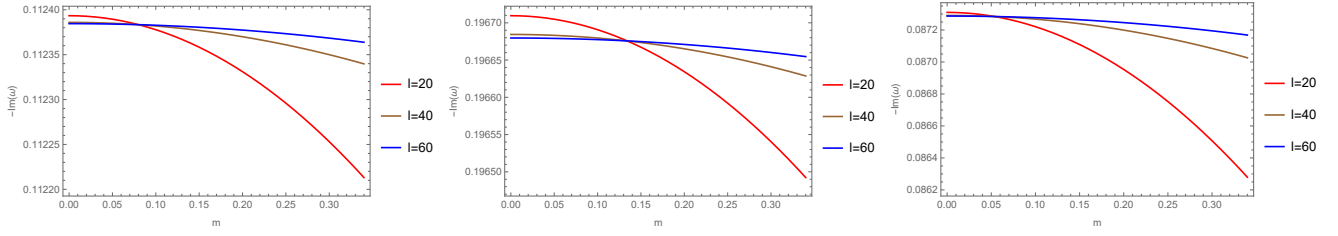


FIG. 8: The behaviour of $-Im(\omega)$ for the fundamental mode ($n = 0$) as a function of the scalar field mass m for different values of the parameter $\ell = 20, 40, 60$, with $M = 1$, $k = 0.07$ (left panel), $k = 1.0$ (central panel), and $k = 8.0$ (right panel). Here, the WKB method gives $m_c \approx 0.08$, $m_c \approx 0.13$, and $m_c \approx 0.05$, respectively.

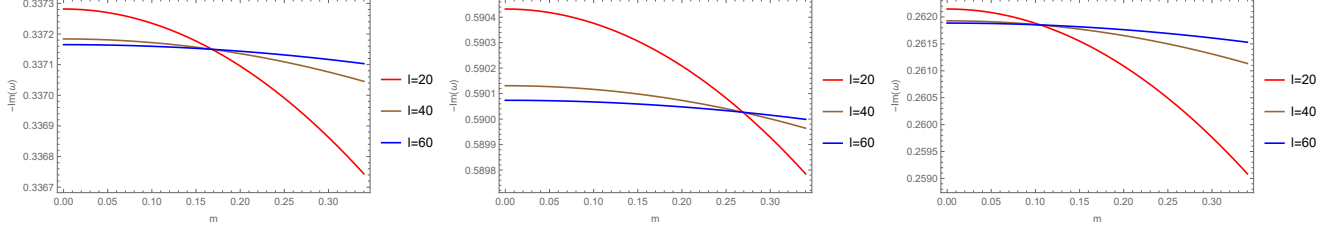


FIG. 9: The behaviour of $-Im(\omega)$ for the first overtone ($n = 1$) as a function of the scalar field mass m for different values of the parameter $\ell = 20, 40, 60$, with $M = 1$, $k = 0.07$ (left panel), $k = 1.0$ (central panel), and $k = 8.0$ (right panel). Here, the WKB method gives $m_c \approx 0.17$, $m_c \approx 0.27$, and $m_c \approx 0.10$, respectively.

Finally, in order to analyze the behaviour of the longest-lived modes with respect to the scalar field mass and the PFDM parameter k , we show in Tables V and VI some fundamental QNFs for $M = 1$, and different values of m , and k . Firstly, it is possible to observe the anomalous behaviour of the decay rate of the QNFs previously described. Bold letters show the longest-lived modes. Additionally, a particular behaviour can be observed for fixed values of the scalar field mass, see $m = 0.08$, and $m = 0.09$. In these cases, for small values of the PFDM parameter k (see $k = 0.01, 0.07$), the longest-lived modes are the one with smallest angular number, then as the k parameter increases (see $k = 1, 2$) the longest-lived modes are the one with highest angular number, and then for biggest values of k (see $k = 5, 10$), the longest-lived modes are the one with smallest angular number.

TABLE V: Fundamental QNFs for $M = 1$, and different values of k and m . Bold letters indicate the longest-lived modes.

k	ℓ	$m = 0$	$m = 0.07$	$m = 0.08$	$m = 0.09$	$m = 0.10$	$m = 0.11$
0.01	20	4.060774422-0.099298049 i	4.060975957-0.099289838 i	4.061037652-0.099287324 i	4.061107574-0.099284475 i	4.061185722-0.099281291 i	4.061272097-0.099277772 i
	40	8.022042946-0.099291809 i	8.022145063-0.099289704 i	8.022176324-0.099289060 i	8.022211752-0.099288329 i	8.022251349-0.099287513 i	8.022295114-0.099286611 i
	60	11.983414279-0.099290623 i	11.983482651-0.099289679 i	11.983503582-0.099289391 i	11.983527303-0.099289063 i	11.983553815-0.099288697 i	11.983583118-0.099288293 i
0.07	20	4.519531072-0.112393405 i	4.519716287-0.112385764 i	4.519772985-0.112383426 i	4.519837244-0.112380775 i	4.519909064-0.112377812 i	4.519988443-0.1123745378 i
	40	8.928296798-0.112385968 i	8.928390648-0.112384009 i	8.928419377-0.112383409 i	8.928451938-0.112382730 i	8.928488329-0.112381970 i	8.928528551-0.112381131 i
	60	13.337180946-0.112384554 i	13.337243784-0.112383676 i	13.337263020-0.112383407 i	13.337284821-0.112383103 i	13.337309187-0.112382762 i	13.337336118-0.112382386 i
1	20	6.258068954-0.196709555 i	6.258256572-0.196700346 i	6.258314006-0.196697527 i	6.258379098-0.196694332 i	6.258451849-0.196690761 i	6.258532257-0.196686814 i
	40	12.362318873-0.196684403 i	12.362413986-0.196682041 i	12.362443102-0.196681318 i	12.362476100-0.196680499 i	12.362512981-0.196679583 i	12.362553744-0.196678571 i
	60	18.466831759-0.196679621 i	18.466895449-0.196678562 i	18.466914945-0.196678238 i	18.466937042-0.196677871 i	18.466961737-0.196677460 i	18.466989033-0.196677006 i
2	20	5.321892057-0.185273143 i	5.322151017-0.185259388 i	5.322230291-0.185255177 i	5.322320135-0.185250405 i	5.322420549-0.185245072 i	5.322531533-0.185239177 i
	40	10.512743590-0.185242445 i	10.512874906-0.185238916 i	10.512915105-0.185237836 i	10.512960663-0.185236612 i	10.513011582-0.185235244 i	10.513067860-0.185233732 i
	60	15.703870347-0.185236608 i	15.703958283-0.185235026 i	15.703985202-0.185234542 i	15.704015710-0.185233993 i	15.704049808-0.185233380 i	15.704087494-0.185232702 i
5	20	3.186561101-0.121455537 i	3.187062385-0.121426919 i	3.187215840-0.121418159 i	3.187389757-0.121408231 i	3.187584136-0.121397135 i	3.187798976-0.121384871 i
	40	6.294508804-0.121430476 i	6.294763071-0.121423133 i	6.294840908-0.121420885 i	6.294929123-0.121418337 i	6.295027717-0.121415490 i	6.295136689-0.121412343 i
	60	9.402654865-0.121425710 i	9.402825145-0.121422418 i	9.402877271-0.121421411 i	9.402936348-0.121420269 i	9.403002375-0.121418992 i	9.403075352-0.121417582 i
10	20	1.853977904-0.073298439 i	1.854893653-0.073244586 i	1.855173990-0.073228102 i	1.855491709-0.073209422 i	1.855846810-0.073188545 i	1.856239296-0.073165473 i
	40	3.662177134-0.073281951 i	3.662641688-0.073268131 i	3.662783899-0.073263900 i	3.662945073-0.073259106 i	3.663125208-0.073253747 i	3.663324305-0.073247825 i
	60	5.470500775-0.073278815 i	5.470811889-0.073272620 i	5.470907128-0.073270724 i	5.471015066-0.073268575 i	5.471135703-0.073266173 i	5.471269038-0.073263518 i

TABLE VI: Fundamental QNFs for $M = 1$, and different values of k and m . Bold letters indicate the longest-lived modes.

k	ℓ	$m = 0.12$	$m = 0.13$	$m = 0.14$	$m = 0.15$	$m = 0.30$
0.01	20	4.061366698-0.099273917 i	4.061469527-0.099269727 i	4.061580583-0.099265202 i	4.061699867-0.099260342 i	4.064476621-0.099147190 i
	40	8.022343047-0.099285622 i	8.022395148-0.099284548 i	8.022451417-0.099283388 i	8.022511855-0.099282142 i	8.023918636-0.099253137 i
	60	11.983615211-0.099287850 i	11.983650096-0.099287369 i	11.983687771-0.099286849 i	11.983728237-0.099286290 i	11.984670127-0.099273291 i
0.07	20	4.520075383-0.112370951 i	4.520169884-0.112367053 i	4.520271945-0.112362843 i	4.520381567-0.112358321 i	4.522933357-0.112253048 i
	40	8.928572603-0.112380211 i	8.928620486-0.112379212 i	8.928672200-0.112378132 i	8.928727745-0.112376973 i	8.930020627-0.112349986 i
	60	13.337365613-0.112381974 i	13.337397674-0.112381526 i	13.337432299-0.112381042 i	13.337469489-0.112380522 i	13.338335129-0.112368427 i
1	20	6.258620324-0.196682492 i	6.258716049-0.196677793 i	6.258819432-0.196672719 i	6.258930473-0.196667269 i	6.261515146-0.196540410 i
	40	12.362598389-0.196677462 i	12.362646916-0.196676257 i	12.362699325-0.196674955 i	12.362755617-0.196673557 i	12.364065865-0.196641019 i
	60	8.467018928-0.196676509 i	18.467051422-0.196675969 i	18.467086517-0.196675386 i	18.467124210-0.196674759 i	18.468001568-0.196660175 i
2	20	5.322653087-0.185232721 i	5.322785212-0.185225703 i	5.322927907-0.185218124 i	5.323081173-0.185209984 i	5.326648698-0.185020522 i
	40	10.513129498-0.185232075 i	10.513196496-0.185230275 i	10.513268854-0.185228331 i	10.513346572-0.185226242 i	10.515155538-0.185177635 i
	60	15.704128770-0.185231959 i	15.704173636-0.185231153 i	15.704222090-0.185230281 i	15.704274134-0.185229345 i	15.705485500-0.185207557 i
5	20	3.188034279-0.121371440 i	3.188290044-0.121356841 i	3.188566272-0.121341075 i	3.188862964-0.121324141 i	3.195769311-0.120930137 i
	40	6.295256040-0.121408896 i	6.295385769-0.121405150 i	6.295525877-0.121401104 i	6.295676363-0.121396758 i	6.299179135-0.121295618 i
	60	9.403155279-0.1214160367 i	9.403242157-0.121414357 i	9.403335985-0.121412544 i	9.403436763-0.121410596 i	9.405782484-0.121365256 i
10	20	1.856669167-0.073140205 i	1.857136425-0.073112743 i	1.857641073-0.073083086 i	1.858183112-0.073051236 i	1.870802383-0.072310891 i
	40	3.663542365-0.073241339 i	3.663779387-0.073234288 i	3.664035373-0.073226674 i	3.664310321-0.073218497 i	3.670710327-0.073028218 i
	60	5.471415072-0.073260610 i	5.471573805-0.073257449 i	5.471745237-0.073254036 i	5.471929367-0.073250370 i	5.476215275-0.073165500 i

V. CONCLUSIONS

In this work, we studied the propagation of massive scalar fields in the background of BHs immersed in perfect fluid dark matter through the QNFs by using the WKB method in order to determine if there is an anomalous decay behaviour in the QNMs as it was observed in other BH backgrounds. Here, we considered the photon sphere modes in our analysis, which are complex.

Concerning to the photon sphere modes, we showed that there is a value of the parameter $k = k_0$, for which the real part of the QNFs is maximum, which is associated with a reflecting point in the context of BH shadow. Namely, as the PFDM parameter k increases in the interval $k < k_0$, the QNF increases and reach their maximum values at $k = k_0$. Then, for $k > k_0$ the real part of the QNF decreases when the parameter k increases. Remarkably, there is a value of the PFDM parameter k , for which the real part of the QNF is the same that for the Schwarzschild BH, beyond this value of k the frequency of oscillation is smaller than the Schwarzschild case. Also, a similar behaviour occurs for the absolute value of the imaginary part of the QNF. However, there is not a value of k , such that will be possible to recover the QNFs for the Schwarzschild background, i.e the real and imaginary part of the QNFs. Also, for massive scalar field, the real part of the QNFs increases and the absolute value of the imaginary part of the QNFs decreases in comparison with massless scalar field.

We showed the existence of anomalous decay rate of QNMs, i.e, the absolute values of the imaginary part of the QNFs decay when the angular harmonic numbers increase if the mass of the scalar field is smaller than a critical mass. On the contrary they grow when the angular harmonic numbers increase, if the mass of the scalar field is larger than the critical mass and they also increase with the overtone number n , for $\ell \geq n$. Also, the critical scalar field mass decreases when the BH mass M increases, and there is a value of k_c corresponding to a maximal value for the critical scalar field mass. Namely, as the PFDM parameter k increases in the interval $k < k_c$, the m_c increases and reach their maximum values at $k = k_c$. Then, for $k > k_c$ the m_c decreases when the parameter k increases. Remarkably, there is a value of the PFDM parameter k , for which the critical scalar field mass is the same that for the Schwarzschild BH, beyond this value of k the critical scalar field mass is smaller than for the Schwarzschild background.

Also, we have reported a particular behaviour for fixed values of the scalar field mass ($m = 0.08, 0.09$), where for small values of the PFDM parameter k ($k = 0.01, 0.07$), the longest-lived modes are the ones with smallest angular number, then as the k parameter increases ($k = 1, 2$) the longest-lived modes are the ones with highest angular number, and then for biggest values of k ($k = 5, 10$), the longest-lived modes are the ones with smallest angular number. Also, in order to show that the scale of the location of the horizon is not important due to the behaviour for $\bar{k} < 1$ is similar to the behaviour for $\bar{k} > 1$, with $\bar{k} = k/r_h$, we have included a dimensionless analysis, see appendix B.

It would be interesting to consider charged black holes immersed in perfect fluid dark matter that represent to the RN dS BHs when the PFDM parameter $k \rightarrow 0$, in order to analyze if it is possible to avoid the existence of unstable modes for $\ell = 0$ for a value of the parameter k for charged massive scalar field. Also, to study the superradiance, as well as, the existence of bound states which could to trigger an instability, work in this direction is in progress.

Appendix A: Higher order derivatives of the potential

In order to explicitly set forth the terms of the WKB approximation outlined in Section IV, we present the higher order derivatives $V^{(i)}(r^*_{max})$ with $i = 2, 3, 4, 5, 6$ of the potential.

$$\begin{aligned}
V^{(0)} &= V_{02}L^2 + V_{00} + \mathcal{O}(L^{-2}), \\
V^{(2)} &= V_{22}L^2 + V_{20} + \mathcal{O}(L^{-2}), \\
V^{(3)} &= V_{32}L^2 + \mathcal{O}(L^0), \\
V^{(4)} &= V_{42}L^2 + \mathcal{O}(L^0), \\
V^{(5)} &= V_{52}L^2 + \mathcal{O}(L^0), \\
V^{(6)} &= V_{62}L^2 + \mathcal{O}(L^0),
\end{aligned} \tag{A1}$$

where

$$V_{00} = \frac{\eta(-\eta + k + m^2r_0^3 + 4M - 3r_1 - r_0) - (2M - r_0)(k + m^2r_0^3 + 2M) + r_1(k + 6M - 2r_0)}{r_0^4}, \tag{A2}$$

$$V_{02} = \frac{-2M + r_0 + \eta}{r_0^3}, \tag{A3}$$

$$V_{22} = \frac{(\eta - 2M + r_0)(k^2 + \eta(15\eta - 11k + 20(r_0 - 3M)) + 22kM - 9kr_0 + 60M^2 - 40Mr_0 + 6r_0^2)}{r_0^7}, \tag{A4}$$

$$\begin{aligned}
V_{20} &= \frac{1}{r_0^9} \left(r_0r_1(-8\eta + k + 16M - 7r_0)(k^2 + \eta(15\eta - 11k + 20(r_0 - 3M)) + 22kM - 9kr_0 + 60M^2 - 40Mr_0 + 6r_0^2) \right. \\
&\quad - r_0(-\eta + 2M - r_0) \left(k^3 + \eta \left(-18k^2 + \eta(-24\eta + 48k + 3m^2r_0^3 + 144M - 35r_0 + 15r_1) \right. \right. \\
&\quad \left. \left. + k(-5m^2r_0^3 - 192M + 64r_0 + 19r_1) - 4M(3m^2r_0^3 - 35r_0 + 15r_1) + 2r_0(m^2r_0^3 - 6r_0 + 20r_1) \right. \right. \\
&\quad \left. \left. - 288M^2 \right) + k^2(m^2r_0^3 + 36M - 15r_0 - 10r_1) + k \left(2M(5m^2r_0^3 - 64r_0 - 19r_1) + r_0(-3m^2r_0^3 + 19r_0 + 2r_1) \right. \right. \\
&\quad \left. \left. + 192M^2 \right) + 4M^2(3m^2r_0^3 - 35r_0 + 15r_1) - 4Mr_0(m^2r_0^3 - 6r_0 + 20r_1) + 192M^3 + 18r_0^2r_1 \right) \Big), \tag{A5}
\end{aligned}$$

$$\begin{aligned}
V_{32} &= -\frac{1}{r_0^9} (\eta - 2M + r_0) \left(-k^3 + \eta \left(29k^2 + \eta(105\eta - 122k + 210(r_0 - 3M)) + 488kM - 190kr_0 + 1260M^2 \right. \right. \\
&\quad \left. \left. - 840Mr_0 + 130r_0^2 \right) + k^2(26r_0 - 58M) + k(-488M^2 + 380Mr_0 - 71r_0^2) - 840M^3 + 840M^2r_0 \right. \\
&\quad \left. - 260Mr_0^2 + 24r_0^3 \right), \tag{A6}
\end{aligned}$$

$$\begin{aligned}
V_{42} = & \frac{1}{r_0^{11}}(\eta - 2M + r_0) \left(k^4 + 134k^3M + r_0^2(443k^2 + 5014kM + 9520M^2) + 2508k^2M^2 \right. \\
& + \eta \left(-67k^3 + \eta \left(627k^2 + 3\eta(315\eta - 506k + 840(r_0 - 3M)) + k(9108M - 3441r_0) \right. \right. \\
& \left. \left. + 140(162M^2 - 108Mr_0 + 17r_0^2) \right) + 76k^2(14r_0 - 33M) + k(-18216M^2 + 13764Mr_0 - 2507r_0^2) \right. \\
& \left. + 28(-1080M^3 + 1080M^2r_0 - 340Mr_0^2 + 33r_0^3) \right) - r_0(63k^3 + 2128k^2M + 13764kM^2 + 20160M^3) \\
& \left. + 12144kM^3 - 4r_0^3(145k + 462M) + 15120M^4 + 120r_0^4 \right), \tag{A7}
\end{aligned}$$

$$\begin{aligned}
V_{52} = & -\frac{1}{r_0^{13}}(\eta - 2M + r_0) \left(-k^5 - 290k^4M - 10472k^3M^2 - 103752k^2M^3 + r_0^3(6631k^2 + 62608kM + 105728M^2) \right. \\
& - 2r_0^2(1037k^3 + 25459k^2M + 136464kM^2 + 176400M^3) + \eta \left(145k^4 + 10472k^3M \right. \\
& + r_0^2(25459k^2 + 272928kM + 529200M^2) + 155628k^2M^2 + \eta \left(-2618k^3 + 3\eta \left(4323k^2 + \eta \left(3465\eta - 7141k \right. \right. \right. \\
& \left. \left. - 11550(3M - r_0) \right) + k(57128M - 21150r_0) + 2100(66M^2 - 44Mr_0 + 7r_0^2) \right) + k^2(31787r_0 - 77814M) \\
& \left. - 12k(42846M^2 - 31725Mr_0 + 5686r_0^2) - 56(14850M^3 - 14850M^2r_0 + 4725Mr_0^2 - 472r_0^3) \right) \\
& - 2r_0(2341k^3 + 63574k^2M + 380700kM^2 + 554400M^3) + 685536kM^3 - 56r_0^3(559k + 1888M) + 831600M^4 \\
& \left. + 7308r_0^4 \right) + 4r_0(35k^4 + 2341k^3M + 31787k^2M^2 + 126900kM^3 + 138600M^4) - 342768kM^4 \\
& \left. - 232r_0^4(22k + 63M) - 332640M^5 + 720r_0^5 \right), \tag{A8}
\end{aligned}$$

$$\begin{aligned}
V_{62} = & \frac{1}{r_0^{15}} (\eta - 2M + r_0) \left(k^6 + 606k^5M + 38956k^4M^2 + 687280k^3M^3 + 4411392k^2M^4 \right. \\
& + r_0^4 (96087k^2 + 790304kM + 1214640M^2) - 2r_0^3 (26415k^3 + 519972k^2M + 2413912kM^2 + 2821280M^3) \\
& + 8r_0^2 (1037k^4 + 47202k^3M + 512376k^2M^2 + 1763502kM^3 + 1732500M^4) \\
& + \eta \left(-303k^5 + 4k^4(4505r_0 - 9739M) - 24k^3(42955M^2 - 36978Mr_0 + 7867r_0^2) \right. \\
& - 12k^2(735232M^3 - 876564M^2r_0 + 341584Mr_0^2 - 43331r_0^3) + \eta \left(9739k^4 + 12k^3(42955M - 18489r_0) \right. \\
& + 24k^2(275712M^2 - 219141Mr_0 + 42698r_0^2) + \eta \left(-85910k^3 + 3\eta \left(91904k^2 + \eta \left(45045\eta - 113623k \right. \right. \right. \\
& \left. \left. \left. - 180180(3M - r_0) \right) \right) + k(1136230M - 414567r_0) + 11550(234M^2 - 156Mr_0 + 25r_0^2) \right) \\
& + k^2(876564r_0 - 2205696M) - 6k(2272460M^2 - 1658268Mr_0 + 293917r_0^2) \\
& - 3080(7020M^3 - 7020M^2r_0 + 2250Mr_0^2 - 229r_0^3) \left. \right) + 4k \left(6817380M^3 - 7462206M^2r_0 + 2645253Mr_0^2 \right. \\
& \left. - 301739r_0^3 \right) + 420(77220M^4 - 102960M^3r_0 + 49500M^2r_0^2 - 10076Mr_0^3 + 723r_0^4) \\
& - 8k(3408690M^4 - 4974804M^3r_0 + 2645253M^2r_0^2 - 603478Mr_0^3 + 49394r_0^4) \\
& - 48(540540M^5 - 900900M^4r_0 + 577500M^3r_0^2 - 176330M^2r_0^3 + 25305Mr_0^4 - 1338r_0^5) \\
& - r_0(297k^5 + 36040k^4M + 887472k^3M^2 + 7012512k^2M^3 + 19899216kM^4 + 17297280M^5) + 10907808kM^5 \\
& \left. - 4r_0^5(12215k + 32112M) + 8648640M^6 + 5040r_0^6 \right), \tag{A9}
\end{aligned}$$

with

$$\eta = k \log \left(\frac{r_0}{k} \right). \tag{A10}$$

On the other hand, our interest is to evaluate the QNFs for large values of L , so we expand the frequencies as a power series in L . It is important to keep in mind that in the eikonal limit, the leading term is linear in L , and for $k = 0$, we should recover the Schwarzschild black hole frequencies. Next, we consider the following expression in powers of L

$$\omega = \omega_{1m}L + \omega_0 + \omega_1L^{-1} + \omega_2L^{-2} + \mathcal{O}(L^{-3}), \tag{A11}$$

where

$$\omega_{1m} = \frac{1}{r_0} \sqrt{\frac{-2M + r_0 + \eta}{r_0}}, \tag{A12}$$

$$\omega_0 = -\frac{i\sqrt{2}}{4r_0^2} \sqrt{-k^2 - \eta(15\eta - 11k + 20(r_0 - 3M)) - 22kM + 9kr_0 - 60M^2 + 40Mr_0 - 6r_0^2}, \tag{A13}$$

$$\begin{aligned}
\omega_1 = & \frac{1}{38880r_0^{5/2}\sqrt{\eta-2M+r_0}} \left(-52110\eta^2 + 6 \left(-645k^2 + 3240r_1(k+6M-2r_0) - 13905kM + 5959kr_0 \right. \right. \\
& -6480m^2Mr_0^3 + 3240m^2r_0^4 - 34740M^2 + 21000Mr_0 - 2241r_0^2 \left. \right) + \frac{1}{\chi} \left(9k^3(5110M-541k) \right. \\
& +6k^2r_0(12347M-5736k) - 3\eta(7665k^3 + 12347k^2r_0 + 5757kr_0^2 + 700r_0^3) + 14r_0^3(300M-1453k) \\
& +2kr_0^2(17271M-23194k) - 2420r_0^4 \left. \right) + \frac{1}{\chi^2} \left(11 \left(549k^5(k+22M) + 3k^4r_0(13808M-1213k) \right. \right. \\
& +2k^3r_0^2(27635M-8257k) + k^2r_0^3(35628M-23939k) \\
& -\eta(33k^2+47kr_0+16r_0^2)(183k^3+367k^2r_0+226kr_0^2+40r_0^3) + 40r_0^5(32M-129k) + kr_0^4(10992M-16145k) \\
& \left. \left. -624r_0^6 \right) \right) + 45\eta(927k+8(54m^2r_0^3+579M-175r_0-162r_1)) \left. \right), \tag{A14}
\end{aligned}$$

with

$$\chi = k^2 + \eta(15\eta - 11k + 20(r_0 - 3M)) + 22kM - 9kr_0 + 60M^2 - 40Mr_0 + 6r_0^2. \tag{A15}$$

$$\begin{aligned}
\omega_2 = & \mu^{-1}i \left(216r_0\delta^6 - 1728 \left((m^2r_0^3 - r_0 + k + 4M - \eta - 3r_1)\eta - (2M - r_0)(m^2r_0^3 + k + 2M) \right. \right. \\
& + (k + 6M - 2r_0)r_1 \left. \right) r_0\delta^5 - 108r_0\alpha\delta^4 + 1728 \left(r_0r_1(k + 16M - 8\eta - 7r_0)\delta \right. \\
& - r_0(2M - \eta - r_0) \left(k^3 + (m^2r_0^3 - 15r_0 + 36M - 10r_1)k^2 + \left(192M^2 + 2(5m^2r_0^3 - 64r_0 - 19r_1)M \right. \right. \\
& + r_0(-3m^2r_0^3 + 19r_0 + 2r_1) \left. \right) k + 192M^3 + \eta \left(-18k^2 + (-5m^2r_0^3 + 64r_0 - 192M + 19r_1)k \right. \\
& - 288M^2 + \eta(3m^2r_0^3 - 35r_0 + 48k + 144M - 24\eta + 15r_1) - 4M(3m^2r_0^3 - 35r_0 + 15r_1) \\
& + 2r_0(m^2r_0^3 - 6r_0 + 20r_1) \left. \right) + 18r_0^2r_1 + 4M^2(3m^2r_0^3 - 35r_0 + 15r_1) - 4Mr_0(m^2r_0^3 - 6r_0 + 20r_1) \left. \right) \delta^4 \\
& + 132\sigma^2r_0\delta^3 + 36 \left(k^6 + 606Mk^5 + 38956M^2k^4 + 687280M^3k^3 + 4411392M^4k^2 + 10907808M^5k + 8648640M^6 \right. \\
& + 5040r_0^6 - 4(12215k + 32112M)r_0^5 + (96087k^2 + 790304Mk + 1214640M^2)r_0^4 \\
& - 2(26415k^3 + 519972Mk^2 + 2413912M^2k + 2821280M^3)r_0^3 + 8 \left(1037k^4 + 47202Mk^3 + 512376M^2k^2 \right. \\
& + 1763502M^3k + 1732500M^4 \left. \right) r_0^2 + \eta \left(-303k^5 + 4(4505r_0 - 9739M)k^4 - 24 \left(42955M^2 - 36978r_0M \right. \right. \quad (A16) \\
& + 7867r_0^2) k^3 - 12(735232M^3 - 876564r_0M^2 + 341584r_0^2M - 43331r_0^3) k^2 - 8 \left(3408690M^4 - 4974804r_0M^3 \right. \\
& + 2645253r_0^2M^2 - 603478r_0^3M + 49394r_0^4) k + \eta \left(9739k^4 + 12(42955M - 18489r_0)k^3 \right. \\
& + 24(275712M^2 - 219141r_0M + 42698r_0^2) k^2 + 4(6817380M^3 - 7462206r_0M^2 + 2645253r_0^2M - 301739r_0^3) k \\
& + \eta \left(-85910k^3 + (876564r_0 - 2205696M)k^2 - 6(2272460M^2 + 293917r_0^2 - 1658268Mr_0)k \right. \\
& + 3\eta \left(91904k^2 + (1136230M - 414567r_0)k + \eta(-113623k + 45045\eta - 180180(3M - r_0)) \right. \\
& + 11550(234M^2 - 156r_0M + 25r_0^2) \left. \right) - 3080(7020M^3 - 7020r_0M^2 + 2250r_0^2M - 229r_0^3) \left. \right) \\
& + 420(77220M^4 - 102960r_0M^3 + 49500r_0^2M^2 - 10076r_0^3M + 723r_0^4) \left. \right) - 48 \left(540540M^5 - 900900r_0M^4 \right. \\
& + 577500r_0^2M^3 - 176330r_0^3M^2 + 25305r_0^4M - 1338r_0^5) \left. \right) - \left(297k^5 + 36040Mk^4 + 887472M^2k^3 \right. \\
& + 7012512M^3k^2 + 19899216M^4k + 17297280M^5) r_0 \left. \right) r_0\delta^3 - 63r_0\alpha^2\delta^2 - 156r_0\sigma \left(-k^5 - 290Mk^4 - 10472M^2k^3 \right. \\
& - 103752M^3k^2 - 342768M^4k - 332640M^5 + 720r_0^5 - 232(22k + 63M)r_0^4 + (6631k^2 + 62608Mk + 105728M^2) r_0^3 \\
& - 2(1037k^3 + 25459Mk^2 + 136464M^2k + 176400M^3) r_0^2 + \eta \left(145k^4 + 10472Mk^3 + 155628M^2k^2 + 685536M^3k \right. \\
& + 831600M^4 + 7308r_0^4 - 56(559k + 1888M)r_0^3 + (25459k^2 + 272928Mk + 529200M^2) r_0^2 \\
& + \eta \left(-2618k^3 + (31787r_0 - 77814M)k^2 - 12(42846M^2 - 31725r_0M + 5686r_0^2)k \right. \\
& + 3\eta(4323k^2 + (57128M - 21150r_0)k + \eta(-7141k + 3465\eta - 11550(3M - r_0)) + 2100(66M^2 - 44r_0M + 7r_0^2)) \\
& - 56(14850M^3 - 14850r_0M^2 + 4725r_0^2M - 472r_0^3) \left. \right) - 2(2341k^3 + 63574Mk^2 + 380700M^2k + 554400M^3) r_0 \left. \right)
\end{aligned}$$

with

$$\mu = 6912r_0^4(-2M + \eta + r_0)\delta^4\sqrt{-2\delta}, \quad (\text{A17})$$

$$\xi = 15\eta - 11k + 20(r_0 - 3M), \quad (\text{A18})$$

$$\delta = \eta\xi + k^2 + 22kM - 9kr_0 + 60M^2 - 40Mr_0 + 6r_0^2, \quad (\text{A19})$$

$$\begin{aligned} \sigma = & -k^3 + \eta(29k^2 + \eta(105\eta - 122k + 210(r_0 - 3M)) + 488kM - 190kr_0 + 1260M^2 - 840Mr_0 + 130r_0^2) \\ & + k^2(26r_0 - 58M) + k(-488M^2 + 380Mr_0 - 71r_0^2) - 840M^3 + 840M^2r_0 - 260Mr_0^2 + 24r_0^3, \end{aligned} \quad (\text{A20})$$

$$\begin{aligned} \alpha = & k^4 + 134k^3M + r_0^2(443k^2 + 5014kM + 9520M^2) + 2508k^2M^2 \\ & + \eta\left(-67k^3 + \eta\left(627k^2 + 3\eta(315\eta - 506k + 840(r_0 - 3M)) + k(9108M - 3441r_0)\right.\right. \\ & \left.\left.+ 140(162M^2 - 108Mr_0 + 17r_0^2)\right) + 76k^2(14r_0 - 33M) + k(-18216M^2 + 13764Mr_0 - 2507r_0^2)\right. \\ & \left.+ 28(-1080M^3 + 1080M^2r_0 - 340Mr_0^2 + 33r_0^3)\right) - r_0(63k^3 + 2128k^2M + 13764kM^2 + 20160M^3) \\ & + 12144kM^3 - 4r_0^3(145k + 462M) + 15120M^4 + 120r_0^4. \end{aligned} \quad (\text{A21})$$

Appendix B: Dimensionless analysis.

Scaling by the event horizon radius r_h , that is, by considering $\bar{r} = r/r_h$, $\bar{k} = k/r_h$, and $\bar{m} = mr_h$. The metric function and the effective potential can be written as

$$f(\bar{r}) = 1 - \frac{1}{\bar{r}} + \frac{\bar{k}}{\bar{r}} \ln(\bar{r}), \quad (\text{B1})$$

$$\bar{V}_{eff}(\bar{r}) = \frac{f(\bar{r})}{\bar{r}^2} (\kappa^2 + \bar{m}^2\bar{r}^2 + \bar{r}f'(\bar{r})) = r_h^2 V_{eff}(r), \quad (\text{B2})$$

respectively. Here, the prime denotes a derivative with respect to \bar{r} . In Fig. 10, we show the behaviour of the effective potential for different values of the parameters. Note that a barrier of potential occurs in each case, with its maximum value increasing when ℓ or \bar{m} increases. However, $\bar{V}_{eff}(\bar{r})$ has a different behaviour than $V_{eff}(r)$, the maximum value of the barrier of potential increases when \bar{k} increases.

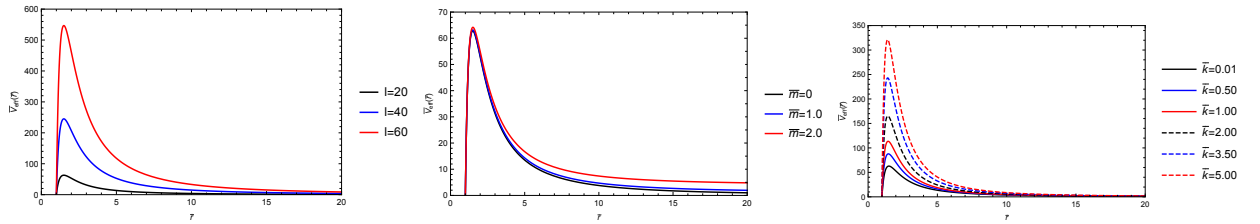


FIG. 10: The effective potential \bar{V}_{eff} as a function of \bar{r} . Left panel for massless scalar field $\bar{m} = 0$, $\bar{k} = 0.01$, and $\ell = 20, 40, 60$. Central panel for $\ell = 20$, $\bar{k} = 0.01$, and $\bar{m} = 0, 1.0, 2.0$. Right panel for $\ell = 20$, $\bar{m} = 0$, and $\bar{k} = 0.01, 0.50, 1.00, 2.00, 3.50, 5.00$.

Also, it is possible to find the critical mass parameter \bar{m}_c , which for small values of \bar{k} is given perturbatively by the expansion

$$\begin{aligned} \bar{m}_c = & \frac{1}{27} \sqrt{\frac{137}{10}} + \bar{k} \left(\frac{77}{30\sqrt{1370}} + \frac{1}{27} \sqrt{\frac{137}{10}} \ln\left(\frac{3}{2}\right) \right) \\ & + \bar{k}^2 \left(-\frac{450343}{277425\sqrt{1370}} + \frac{1}{27} \sqrt{\frac{137}{10}} \ln^2\left(\frac{3}{2}\right) + \frac{4}{135} \sqrt{\frac{2}{685}} \ln\left(\frac{3}{2}\right) \right) + O(\bar{k}^3). \end{aligned} \quad (\text{B3})$$

We plot its behaviour as a function of \bar{k} in Fig. 11. We can observe that when the parameter \bar{k} increases the critical mass \bar{m}_c increases and also for $\bar{k} = 0$ we recover the value of Schwarzschild black hole.

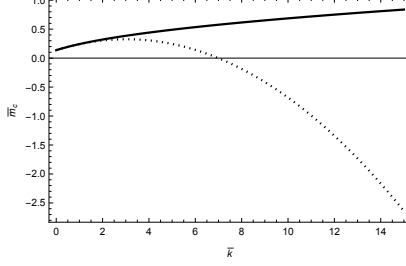


FIG. 11: The behaviour of the critical scalar field mass \bar{m}_c for the fundamental mode $n = 0$ as a function of \bar{k} . Continuous line for the exact value of \bar{m}_c , and dotted line for approximate expression of \bar{m}_c via Eq. (B3).

Now, we plot in Fig. 12 the behaviour of the real and imaginary parts of $\bar{\omega} = \omega r_h$ as a function of the parameter \bar{k} , separately. Here, both the real part and absolute value of the imaginary part of $\bar{\omega}$ increase when the parameter \bar{k} or \bar{m} increases, i.e. there is a corresponding elevation in both oscillation frequency and damping. Specifically, when $\bar{k} > 1$, it signifies a scenario predominantly governed by dark matter, as this condition is equivalent to $k > r_h$. In this context, the influence of dark matter manifests as an augmentation in both the oscillation frequency and damping of the QNFs.

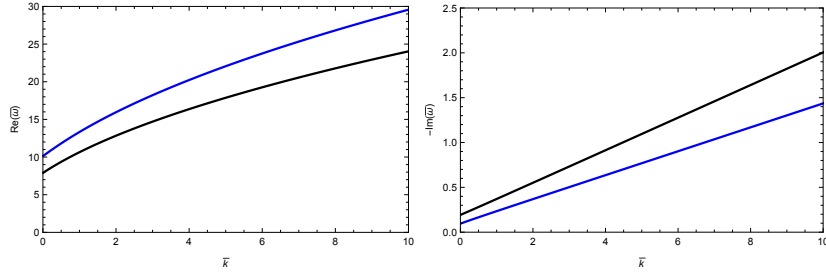


FIG. 12: The behaviour of $Re(\bar{\omega})$ (left panel), and $Im(\bar{\omega})$ (right panel) for the fundamental mode ($n = 0$) as a function of the parameter \bar{k} , and $\ell = 20$. Black line for $\bar{m} = 0$, and blue line for $\bar{m} = 10$.

Now, in order to show the anomalous behaviour, we plot in Fig. 13, and 14, the behaviour of $-Im(\bar{\omega})$ as a function of \bar{m} by using the 6th order WKB method for $n = 0$, and $n = 1$, respectively. We can observe an anomalous decay rate, i.e. for $\bar{m} < \bar{m}_c$, the longest-lived modes are the one with highest angular number ℓ ; whereas, for $\bar{m} > \bar{m}_c$, the longest-lived modes are the one with smallest angular number. Also, when the overtone number n increases the parameter \bar{m}_c increases. Also, it is possible to observe that the behaviour of the critical parameter \bar{m}_c with respect to the parameter \bar{k} agrees with Fig. 11.

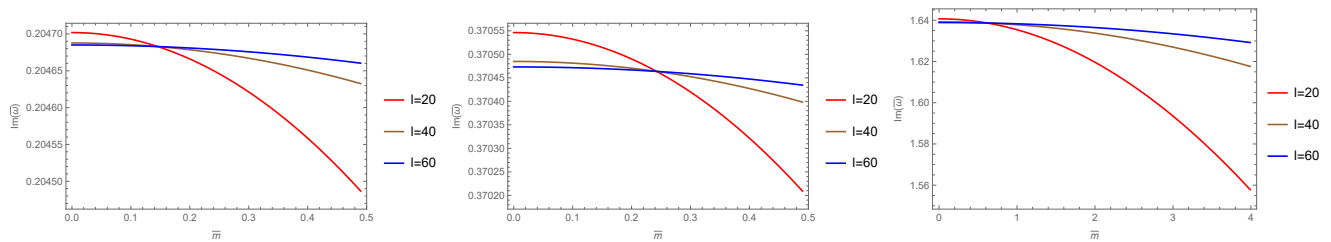


FIG. 13: The behaviour of $-Im(\bar{\omega})$ for the fundamental mode ($n = 0$) as a function of \bar{m} for different values of the parameter $\ell = 20, 40, 60$, with $\bar{k} = 0.07$ (left panel), $\bar{k} = 1.0$ (central panel), and $\bar{k} = 8.0$ (right panel). Here, the WKB method gives $\bar{m}_c \approx 0.15$, $\bar{m}_c \approx 0.24$, and $\bar{m}_c \approx 0.62$, respectively.

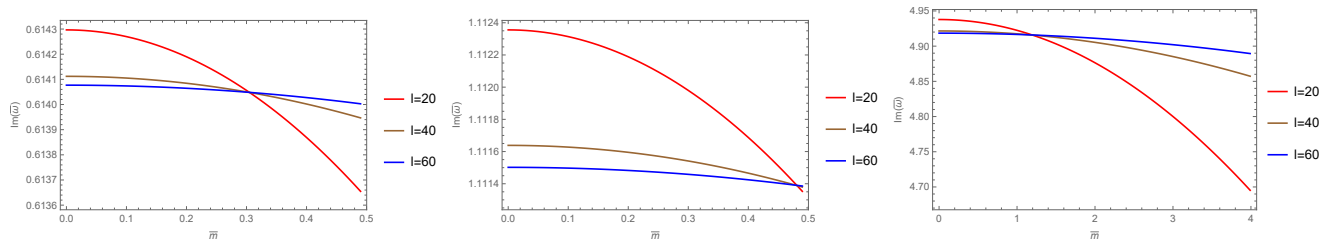


FIG. 14: The behaviour of $-Im(\bar{\omega})$ for the first overtone ($n = 1$) as a function of \bar{m} for different values of the parameter $\ell = 20, 40, 60$, with $M = 1$, $\bar{k} = 0.07$ (left panel), $\bar{k} = 1.0$ (central panel), and $\bar{k} = 8.0$ (right panel). Here, the WKB method gives $\bar{m}_c \approx 0.30$, $\bar{m}_c \approx 0.48$, and $\bar{m}_c \approx 1.19$, respectively.

The above description of $\bar{V}_{eff}(\bar{r})$, \bar{m}_c , $Re(\bar{\omega})$, $Im(\bar{\omega})$ show that the scale of the location of the horizon is not important, due to the behaviour for $\bar{k} < 1$ is similar to the behaviour for $\bar{k} > 1$, with $\bar{k} = k/r_h$.

Acknowledgments

We thank the referee for his/her constructive comments as well as for useful comments and suggestions. We thank Kyriakos Destounis for carefully reading the manuscript and for his comments and suggestions. This work is partially supported by ANID Chile through FONDECYT Grant N^o 1220871 (P.A.G., and Y. V.). P. A. G. acknowledges the hospitality of the Universidad de La Serena where part of this work was undertaken.

-
- [1] LIGO Scientific and Virgo Collaborations collaboration, B. P. Abbott et al., Observation of Gravitational Waves from a Binary Black Hole Merger, *Phys. Rev. Lett.* **116** (2016) 061102.
 - [2] VGW151226: Observation of Gravitational Waves from a 22-Solar-Mass Binary Black Hole Coalescence, *Phys. Rev. Lett.* **116** (2016) 241103.
 - [3] VIRGO, LIGO SCIENTIFIC collaboration, B. P. Abbott et al., GW170104: Observation of a 50-Solar-Mass Binary Black Hole Coalescence at Redshift 0.2, *Phys. Rev. Lett.* **118** (2017) 221101.
 - [4] Virgo, LIGO Scientific collaboration, B. P. Abbott et al., GW170814: A Three-Detector Observation of Gravitational Waves from a Binary Black Hole Coalescence, *Phys. Rev. Lett.* **119** (2017) 141101.
 - [5] Virgo, LIGO Scientific collaboration, B. P. Abbott et al., GW170817: Observation of Gravitational Waves from a Binary Neutron Star Inspiral, *Phys. Rev. Lett.* **119** (2017) 161101.
 - [6] C. V. Vishveshwara, "Scattering of Gravitational Radiation by a Schwarzschild Black-hole," *Nature* **227**, 936 (1970).
 - [7] K. D. Kokkotas and B. G. Schmidt, "Quasinormal modes of stars and black holes," *Living Rev. Rel.* **2**, 2 (1999) [gr-qc/9909058].
 - [8] E. Berti, V. Cardoso and A. O. Starinets, "Quasinormal modes of black holes and black branes," *Class. Quant. Grav.* **26**, 163001 (2009) [arXiv:0905.2975 [gr-qc]].
 - [9] R. A. Konoplya and A. Zhidenko, "Quasinormal modes of black holes: From astrophysics to string theory," *Rev. Mod. Phys.* **83**, 793 (2011) [arXiv:1102.4014 [gr-qc]].

- [10] V. Cardoso, E. Franzin and P. Pani, “Is the gravitational-wave ringdown a probe of the event horizon?,” *Phys. Rev. Lett.* **116** (2016) no.17, 171101 [arXiv:1602.07309 [gr-qc]].
- [11] V. Cardoso, S. Hopper, C. F. B. Macedo, C. Palenzuela and P. Pani, “Gravitational-wave signatures of exotic compact objects and of quantum corrections at the horizon scale,” *Phys. Rev. D* **94** (2016) no.8, 084031 [arXiv:1608.08637 [gr-qc]].
- [12] F. Ferrer, A. Medeiros da Rosa, and C. M. Will, “Dark matter spikes in the vicinity of kerr black holes,” *Phys.Rev. D* **96**, 083014 (2017).
- [13] S. Nampalliwar, S. Kumar, K. Jusufi, Q. Wu, M. Jamil, and P. Salucci, “Modeling the sgr a* black hole immersed in a dark matter spike,” *The Astrophysical Journal* **916**,116 (2021).
- [14] Z. Xu, J. Wang, and M. Tang, “Deformed black hole immersed in dark matter spike,” *Journal of Cosmology and Astroparticle Physics* **2021** (09), 007.
- [15] K. Jusufi, M. Jamil, and T. Zhu, “Shadows of black hole surrounded by superfluid dark matter halo,“ *The European Physical Journal C* **80**, 354 (2020).
- [16] G. Battaglia, A. Helmi, H. Morrison, P. Harding, E. W. Olszewski, M. Mateo, K. C. Freeman, J. Norris and S. A. Shtetman, “The Radial velocity dispersion profile of the Galactic Halo: Constraining the density profile of the dark halo of the Milky Way,” *Mon. Not. Roy. Astron. Soc.* **364** (2005), 433-442 [erratum: *Mon. Not. Roy. Astron. Soc.* **370** (2006), 1055] [arXiv:astro-ph/0506102 [astro-ph]].
- [17] P. R. Kafle, S. Sharma, G. F. Lewis and J. Bland-Hawthorn, “On the Shoulders of Giants: Properties of the Stellar Halo and the Milky Way Mass Distribution,” *Astrophys. J.* **794** (2014) no.1, 59 [arXiv:1408.1787 [astro-ph.GA]].
- [18] X. Hou, Z. Xu and J. Wang, “Rotating Black Hole Shadow in Perfect Fluid Dark Matter,” *JCAP* **12** (2018), 040 [arXiv:1810.06381 [gr-qc]].
- [19] S. Haroon, M. Jamil, K. Jusufi, K. Lin and R. B. Mann, “Shadow and Deflection Angle of Rotating Black Holes in Perfect Fluid Dark Matter with a Cosmological Constant,” *Phys. Rev. D* **99** (2019) no.4, 044015 [arXiv:1810.04103 [gr-qc]].
- [20] X. Hou, Z. Xu, M. Zhou and J. Wang, “Black hole shadow of Sgr A* in dark matter halo,” *JCAP* **07** (2018), 015 [arXiv:1804.08110 [gr-qc]].
- [21] K. Jusufi, “Black holes surrounded by Einstein clusters as models of dark matter fluid,” *Eur. Phys. J. C* **83**, no.2, 103 (2023) [arXiv:2202.00010 [gr-qc]].
- [22] R. A. Konoplya and A. Zhidenko, “Solutions of the Einstein Equations for a Black Hole Surrounded by a Galactic Halo,” *Astrophys. J.* **933**, no.2, 166 (2022) [arXiv:2202.02205 [gr-qc]].
- [23] E. Figueiredo, A. Maselli and V. Cardoso, “Black holes surrounded by generic dark matter profiles: Appearance and gravitational-wave emission,” *Phys. Rev. D* **107**, no.10, 104033 (2023) [arXiv:2303.08183 [gr-qc]].
- [24] S. V. M. C. B. Xavier, H. C. D. Lima, Junior. and L. C. B. Crispino, “Shadows of black holes with dark matter halo,” *Phys. Rev. D* **107**, no.6, 064040 (2023) [arXiv:2303.17666 [gr-qc]].
- [25] S. Perlmutter *et al.* [Supernova Cosmology Project Collaboration], *Astrophys. J.* **517**, 565 (1999) [arXiv:astro-ph/9812133]; A. G. Riess *et al.* [Supernova Search Team Collaboration], *Cosmological Constant*, *Astron. J.* **116**, 1009 (1998) [arXiv:astro-ph/9805201]; P. M. Garnavich *et al.*, *Astrophys. J.* **509**, 74 (1998) [arXiv:astro-ph/9806396].
- [26] E. Komatsu *et al.* [WMAP], “Seven-Year Wilkinson Microwave Anisotropy Probe (WMAP) Observations: Cosmological Interpretation,” *Astrophys. J. Suppl.* **192**, 18 (2011) [arXiv:1001.4538 [astro-ph.CO]].
- [27] U. Alam, V. Sahni, T. D. Saini and A. A. Starobinsky, “Is there supernova evidence for dark energy metamorphosis?,” *Mon. Not. Roy. Astron. Soc.* **354**, 275 (2004) [arXiv:astro-ph/0311364 [astro-ph]].
- [28] R. R. Caldwell, “A Phantom menace?,” *Phys. Lett. B* **545**, 23-29 (2002) [arXiv:astro-ph/9908168 [astro-ph]].
- [29] R. R. Caldwell, M. Kamionkowski and N. N. Weinberg, “Phantom energy and cosmic doomsday,” *Phys. Rev. Lett.* **91**, 071301 (2003) [arXiv:astro-ph/0302506 [astro-ph]].
- [30] S. Nesseris and L. Perivolaropoulos, “The Fate of bound systems in phantom and quintessence cosmologies,” *Phys. Rev. D* **70**, 123529 (2004) [arXiv:astro-ph/0410309 [astro-ph]].
- [31] Á. O. F. de Almeida, L. Amendola and V. Niro, “Galaxy rotation curves in modified gravity models,” *JCAP* **08**, 012 (2018) [arXiv:1805.11067 [astro-ph.GA]].
- [32] J. Harada, “Cotton gravity and 84 galaxy rotation curves,” *Phys. Rev. D* **106**, no.6, 064044 (2022) [arXiv:2209.04055 [gr-qc]].
- [33] H. Shabani and P. H. R. S. Moraes, “Galaxy rotation curves in the f(R, T) gravity formalism,” *Phys. Scripta* **98**, no.6, 065302 (2023) [arXiv:2206.14920 [gr-qc]].
- [34] R. A. Konoplya, Z. Stuchlík and A. Zhidenko, “Echoes of compact objects: new physics near the surface and matter at a distance,” *Phys. Rev. D* **99** (2019) no.2, 024007 [arXiv:1810.01295 [gr-qc]].
- [35] E. Barausse, V. Cardoso and P. Pani, “Can environmental effects spoil precision gravitational-wave astrophysics?,” *Phys. Rev. D* **89** (2014) no.10, 104059 [arXiv:1404.7149 [gr-qc]].
- [36] P. T. Leung, Y. T. Liu, W. M. Suen, C. Y. Tam and K. Young, “Quasinormal modes of dirty black holes,” *Phys. Rev. Lett.* **78** (1997), 2894-2897 [arXiv:gr-qc/9903031 [gr-qc]].
- [37] R. A. Konoplya, “Shadow of a black hole surrounded by dark matter,” *Phys. Lett. B* **795** (2019), 1-6 [arXiv:1905.00064 [gr-qc]].
- [38] V. Cardoso, K. Destounis, F. Duque, R. P. Macedo and A. Maselli, *Phys. Rev. D* **105**, no.6, L061501 (2022) [arXiv:2109.00005 [gr-qc]].
- [39] V. Cardoso, K. Destounis, F. Duque, R. Panosso Macedo and A. Maselli, “Gravitational Waves from Extreme-Mass-Ratio Systems in Astrophysical Environments,” *Phys. Rev. Lett.* **129**, no.24, 241103 (2022) [arXiv:2210.01133 [gr-qc]].

- [40] V. V. Kiselev, “Quintessence and black holes,” *Class. Quant. Grav.* **20**, 1187-1198 (2003) [arXiv:gr-qc/0210040 [gr-qc]].
- [41] V. V. Kiselev, “Quintessential solution of dark matter rotation curves and its simulation by extra dimensions,” [arXiv:gr-qc/0303031 [gr-qc]].
- [42] M. H. Li and K. C. Yang, “Galactic Dark Matter in the Phantom Field,” *Phys. Rev. D* **86**, 123015 (2012) [arXiv:1204.3178 [astro-ph.CO]].
- [43] V. Cardoso, A. S. Miranda, E. Berti, H. Witek and V. T. Zanchin, “Geodesic stability, Lyapunov exponents and quasinormal modes,” *Phys. Rev. D* **79**, no.6, 064016 (2009) [arXiv:0812.1806 [hep-th]].
- [44] A. Aragón, P. A. González, E. Papantonopoulos and Y. Vásquez, “Anomalous decay rate of quasinormal modes in Schwarzschild-dS and Schwarzschild-AdS black holes,” *JHEP* **08** (2020), 120 [arXiv:2004.09386 [gr-qc]].
- [45] A. Aragón, P. A. González, E. Papantonopoulos and Y. Vásquez, “Quasinormal modes and their anomalous behavior for black holes in $f(R)$ gravity,” *Eur. Phys. J. C* **81** (2021) no.5, 407 [arXiv:2005.11179 [gr-qc]].
- [46] R. D. B. Fontana, P. A. González, E. Papantonopoulos and Y. Vásquez, “Anomalous decay rate of quasinormal modes in Reissner-Nordström black holes,” *Phys. Rev. D* **103** (2021) no.6, 064005 [arXiv:2011.10620 [gr-qc]].
- [47] R. Bécar, P. A. González, F. Moncada and Y. Vásquez, “Massive scalar field perturbations in Weyl black holes,” [arXiv:2304.00663 [gr-qc]].
- [48] R. A. Konoplya and A. V. Zhidenko, “Decay of massive scalar field in a Schwarzschild background,” *Phys. Lett. B* **609** (2005), 377-384 [arXiv:gr-qc/0411059 [gr-qc]].
- [49] R. A. Konoplya and A. Zhidenko, “Stability and quasinormal modes of the massive scalar field around Kerr black holes,” *Phys. Rev. D* **73** (2006), 124040 [arXiv:gr-qc/0605013 [gr-qc]].
- [50] S. R. Dolan, “Instability of the massive Klein-Gordon field on the Kerr spacetime,” *Phys. Rev. D* **76** (2007), 084001 [arXiv:0705.2880 [gr-qc]].
- [51] O. J. Tattersall and P. G. Ferreira, “Quasinormal modes of black holes in Horndeski gravity,” *Phys. Rev. D* **97** (2018) no.10, 104047 [arXiv:1804.08950 [gr-qc]].
- [52] M. Lagos, P. G. Ferreira and O. J. Tattersall, “Anomalous decay rate of quasinormal modes,” *Phys. Rev. D* **101** (2020) no.8, 084018 [arXiv:2002.01897 [gr-qc]].
- [53] P. A. González, E. Papantonopoulos, Á. Rincón and Y. Vásquez, “Quasinormal modes of massive scalar fields in four-dimensional wormholes: Anomalous decay rate,” *Phys. Rev. D* **106** (2022) no.2, 024050 [arXiv:2205.06079 [gr-qc]].
- [54] P. A. González, E. Papantonopoulos, J. Saavedra and Y. Vásquez, “Quasinormal modes for massive charged scalar fields in Reissner-Nordström dS black holes: anomalous decay rate,” *JHEP* **06** (2022), 150 [arXiv:2204.01570 [gr-qc]].
- [55] R. Bécar, P. A. González and Y. Vásquez, “Quasinormal modes of a charged scalar field in Ernst black holes,” *Eur. Phys. J. C* **83** (2023) no.1, 75 [arXiv:2211.02931 [gr-qc]].
- [56] A. Aragón, R. Bécar, P. A. González and Y. Vásquez, “Massive Dirac quasinormal modes in Schwarzschild–de Sitter black holes: Anomalous decay rate and fine structure,” *Phys. Rev. D* **103** (2021) no.6, 064006 [arXiv:2009.09436 [gr-qc]].
- [57] K. Destounis, R. D. B. Fontana and F. C. Mena, “Accelerating black holes: quasinormal modes and late-time tails,” *Phys. Rev. D* **102**, no.4, 044005 (2020) [arXiv:2005.03028 [gr-qc]].
- [58] K. Jusufi, “Quasinormal Modes of Black Holes Surrounded by Dark Matter and Their Connection with the Shadow Radius,” *Phys. Rev. D* **101**, no.8, 084055 (2020) [arXiv:1912.13320 [gr-qc]].
- [59] I. Z. Stefanov, S. S. Yazadjiev and G. G. Gylchev, “Connection between Black-Hole Quasinormal Modes and Lensing in the Strong Deflection Limit,” *Phys. Rev. Lett.* **104**, 251103 (2010) [arXiv:1003.1609 [gr-qc]].
- [60] B. Cuadros-Melgar, R. D. B. Fontana and J. de Oliveira, “Analytical correspondence between shadow radius and black hole quasinormal frequencies,” *Phys. Lett. B* **811**, 135966 (2020) [arXiv:2005.09761 [gr-qc]].
- [61] M. A. Anacleto, J. A. V. Campos, F. A. Brito and E. Passos, “Quasinormal modes and shadow of a Schwarzschild black hole with GUP,” *Annals Phys.* **434**, 168662 (2021) [arXiv:2108.04998 [gr-qc]].
- [62] B. Mashhoon, “*Quasi-normal modes of a black hole*,” Third Marcel Grossmann Meeting on General Relativity 1983.
- [63] B. F. Schutz and C. M. Will, “BLACK HOLE NORMAL MODES: A SEMIANALYTIC APPROACH,” *Astrophys. J. Lett.* **291** (1985), L33-L36
- [64] S. Iyer and C. M. Will, “Black Hole Normal Modes: A WKB Approach. 1. Foundations and Application of a Higher Order WKB Analysis of Potential Barrier Scattering,” *Phys. Rev. D* **35** (1987), 3621
- [65] R. A. Konoplya, “Quasinormal behavior of the d-dimensional Schwarzschild black hole and higher order WKB approach,” *Phys. Rev. D* **68** (2003), 024018 [arXiv:gr-qc/0303052 [gr-qc]].
- [66] J. Matyjasek and M. Opala, “Quasinormal modes of black holes. The improved semianalytic approach,” *Phys. Rev. D* **96** (2017) no.2, 024011 [arXiv:1704.00361 [gr-qc]].
- [67] R. A. Konoplya, A. Zhidenko and A. F. Zinhailo, “Higher order WKB formula for quasinormal modes and grey-body factors: recipes for quick and accurate calculations,” *Class. Quant. Grav.* **36** (2019), 155002 [arXiv:1904.10333 [gr-qc]].
- [68] Y. Hatsuda, “Quasinormal modes of black holes and Borel summation,” *Phys. Rev. D* **101** (2020) no.2, 024008 [arXiv:1906.07232 [gr-qc]].